RESEARCH ARTICLE

Key Points:
- Modeling of basin-scale fluid flow shows that tapping hot fluids from deep confined aquifers by faults can produce large Zn deposits
- Heat anomaly that drives the hydrothermal system can form at magma-poor hyperextended continental margins as inferred for the Selwyn Basin
- Modeled metal enrichment agrees with observations from the deposits, but the timescale is much shorter than assumed in classical models

Hydrodynamic Constraints on Ore Formation by Basin-Scale Fluid Flow at Continental Margins: Modelling Zn Metallogenesis in the Devonian Selwyn Basin

Alejandro Rodríguez[1,2] [ID]**, Philipp Weis[1]** [ID]**, Joseph M. Magnall[1]** [ID]**, and Sarah A. Gleeson[1,3]** [ID]

[1]GFZ German Research Centre for Geosciences, Potsdam, Germany, [2]Currently at OVSICORI Observatorio Vulcanológico y Sismológico de Costa Rica, Heredia, Costa Rica, [3]Institute of Geological Sciences, Freie Universität Berlin, Berlin, Germany

Abstract The clastic-dominant (CD-type) deposits that are contained within sedimentary basins are major resources of Zn, Pb and Ag, but their formation by basin-scale hydrothermal mass and energy transport processes is still poorly understood. Using geological constraints from the Late Devonian Selwyn Basin (Canada), we apply quantitative numerical fluid flow modeling to explore the effect of strata permeability, timing of fault opening and increased heat flow in controlling fluid migration, metal leaching and ore formation during an extensional tectonic event. The results indicate that tapping hot fluids from a confined and permeable aquifer at several km depths by means of permeable normal faults is a key factor for the formation of large Zn-Pb deposits. The hot (282°C) ore-forming fluids are transported to the shallow subsurface shortly after the initiation of a rifting event (within 100 kyr), before the development of extensive basin-scale convection patterns that lead to stronger cooling and a reduction in the capacity of the hydrothermal system to make an economic deposit. Such a hydrothermal event can result in metal endowments comparable to the deposits of the Selwyn Basin.

1. Introduction

Continental rifting and the formation of sedimentary basins are fundamentally multiphase processes that result from interactions between the crust and mantle (Peron-Pinvidic et al., 2019). The mineral resources contained within sedimentary basins are, therefore, the end product of geodynamic processes operating on multiple scales, although key aspects of metallogenesis in these settings remain poorly understood. Clastic-dominant (CD-type) deposits (formally known as SEDEX deposits) have the highest grades and tonnages of the sediment-hosted base metal deposits, and contain millions of tonnes of Zn, Pb and reduced sulfur (Leach et al., 2010), yet there are few paleohydrological constraints on the basin-scale controls on mass transfer in these systems. As a result, it is not well understood why exceptional periods of metallogenesis are restricted to a limited number of sedimentary basins in the geological record or which aspects of basin evolution (e.g. rifting, sedimentation, burial) are integral to ore formation.

CD-type deposits are typically hosted by carbonaceous, fine-grained siliciclastic rocks deposited in extensional settings (intracontinental or continental margin) and are not genetically associated with magmatic activity. Faults play a major role in the generation of both accommodation space for the host rock and as a conduit for hydrothermal fluid migration to the shallow subsurface or the seafloor (Cathles & Adams, 2005; Walsh et al., 2018). Traditional genetic models for CD-type deposits have considered sulphide mineralization to be sedimentary exhalative (SEDEX; Large et al., 2005), which involves hydrothermal exhalation of a saline (3–23 wt.% NaCl equiv.), metal-rich fluid from a fault-bound feeder zone (or vent complex). The metals are leached from deep in the basin, and upon exhalation are precipitated as sulphide minerals (pyrite, FeS_2; sphalerite, ZnS; galena, PbS) during fluid mixing with anoxic sulphidic (euxinic) seawater (Goodfellow et al., 1995). Inferred timescales of ore formation in the SEDEX model are long (>Myr), because protracted hydrothermal venting is necessary for the syn-sedimentary accumulation of sulphide minerals (Turner, 1992).

There are very few CD-type deposits where a fossilized vent complex is actually preserved in the geological record. As a result, CD-type deposits have been sub-divided into vent-proximal and vent-distal systems, with the latter considered to form after the migration of hydrothermal fluids away from the site of active

venting onto the seafloor (Sangster, 2018). The fine-grained nature of the mineralization and the paucity of vent or feeder complexes also means there are limited localities where fluid inclusions have been preserved (Magnall et al., 2016; Rajabi et al., 2014) and so the composition of ore-forming fluids is relatively unconstrained in many systems. Nevertheless, a broad framework has been proposed, which follows the use of this limited input data for thermodynamic modeling and involves sub-division of deposits into two groups (Cooke et al., 2000): *McArthur-type*, which formed from oxidising, low-temperature (<150°C), high-salinity (>18 wt.% NaCl equiv.) fluids, and *Selwyn-type*, which formed from reduced, high-temperature (>250°C), intermediate-salinity (<12 wt.% NaCl equiv.) fluids. In both cases the salinity, redox and temperature are considered to have provided a major control on the efficiency of metal transport and deposition.

The North American Cordillera contains two basins with exceptional metal endowment: the Mississippian Kuna Basin which hosts the giant Red Dog deposits and the Selwyn Basin. The Selwyn Basin contains CD-type deposits that formed in the Cambrian, Ordovician-Silurian and Late Devonian (Goodfellow et al., 1995). Recent work on the Late Devonian Tom and Jason deposits (Macmillan Pass) has shown how sub-seafloor replacement (<1 km depth) of diagenetic barite rather than true SEDEX processes could have produced mineralization (Magnall et al., 2020). The deposits at Macmillan Pass are currently subeconomic (which is partly related to the remote location; Figure 1); however, they are high grade (39.5 Mt at 10% Zn equivalent, inferred; Fireweed Zn Resources) and exploration is still underway to determine the overall size of these systems. Moreover, the Macmillan Pass deposits are relatively undeformed and are one of the few localities where feeder complexes are preserved. Therefore, these deposits have commonly been used as the type locality for this mineral system (e.g. Goodfellow et al., 1995). Geochemical and isotopic analyses on feeder complex samples from Macmillan Pass have shown that the metal-bearing fluids were hot (300°C) and low salinity (<6 wt.% NaCl equiv.; Magnall et al., 2016). In the absence of coeval magmatic activity, there are some fundamental outstanding questions relating to how such hot hydrothermal fluids can be generated and migrate to form Macmillan Pass style deposits in the shallow subsurface in ancient marine basins.

Previous studies have evaluated basin-scale paleohydrology of mineral systems using numerical fluid-flow models (Ingebritsen & Appold, 2012 and references therein; Oliver et al., 2006). Tectonic squeezing and sedimentary compaction models have been tested, but results suggest that fluid flow rates from compression are too slow to be an effective driver for fluid flow over large distances (Garven, 1995; Ge & Garven, 1992). Rift basins containing CD-type deposits also lack a sufficiently large hydraulic head for basin-scale topography-driven flow controlled by regional-scale orogenic belts (e.g. Appold & Garven, 1999). Rather, thermal convection has been modeled as an effective mechanism of mass and energy transport in extensional basins (Simms & Garven, 2004; Yang et al., 2006). Thermohaline convection models also show that residual brines from seawater evaporation within shelf carbonate sequences have the potential to laterally migrate into contiguous ocean basins (Manning & Emsbo, 2018). Nevertheless, the relative roles and timing of the potential driving forces of fluid flow remain uncertain, including regional topography, sediment compaction, tectonic deformation, thermal convection, salinity-dependent density gradients and episodic tapping of overpressured fluid reservoirs.

There has been no detailed consideration of the paleohydrological factors that might have imposed a first-order control on CD-type metallogenesis during the evolution of the Selwyn Basin. Previously, the secular distribution of CD-type deposits was linked to periods of basin stagnation and the presence of a favorable metal trap (Goodfellow & Lydon, 2007). For the present study, we describe a numerical model that has been parameterized using recent studies at Macmillan Pass. Our study focusses on the physical hydrology and thermal evolution during an idealized ore-forming event. We further constrain metal fluxes by explicitly taking into account the limiting factors of metal availability in the source rocks and empirical approximations for temperature-dependent metal solubilities in the hydrothermal fluids. We evaluate the effect of the initial pressure distribution, the presence of geological units (aquitard vs. aquifer) and the timing of both fault opening and heat anomaly in the formation of a CD-type deposit. The results show how key aspects of basin evolution (rifting and burial) might have been optimized to result in crustal-scale self-organization of ore-forming processes.
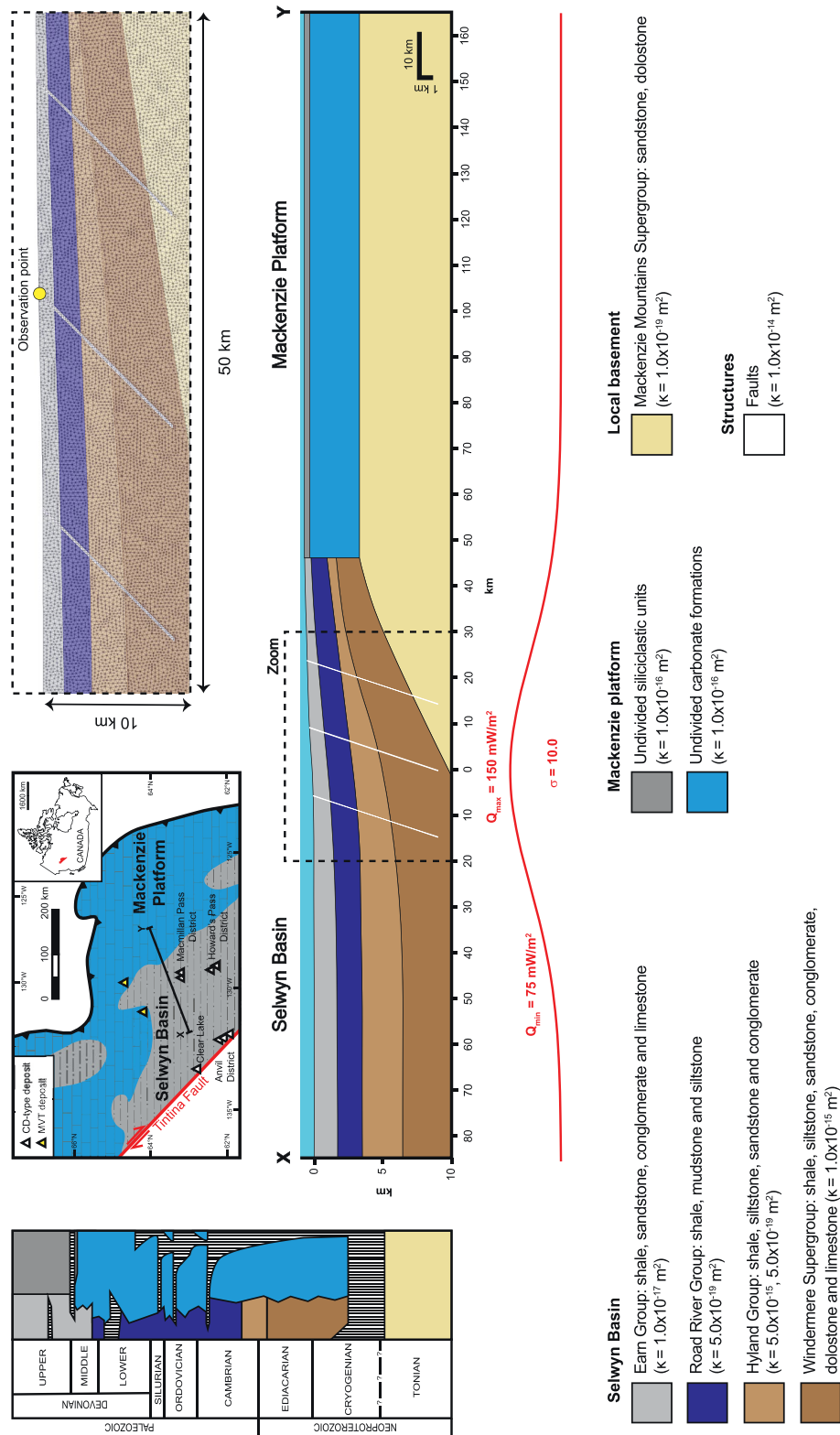
Figure 1

2. Geological Framework and Model Geometry

The Selwyn Basin has an area of $\sim 140 \times 103$ km^2 and is the largest basin of the Canadian Cordillera (Cecile et al., 1997). The earliest stage of basin formation involved Cordilleran rift development during moderate lithospheric stretching and breakup of the Rodinian supercontinent between the early Tonian to Cryogenian (Colpron et al., 2002; Yonkee et al., 2014). Neoproterozoic to Cambrian age sedimentary rocks of the Windermere Supergroup record syn-rift deposition that was associated with Rodinian breakup (Moynihan et al., 2019; Strauss et al., 2015). A passive continental margin then developed along the western margin of ancestral North America (Laurentia; Lund, 2008). Overlying the Windermere Supergroup are extensive platformal carbonate and coeval fine-grained basinal strata of the Hyland Group (Cecile et al., 1997). Between the Mid-Cambrian to Late Devonian, episodic extension and associated subsidence resulted in deposition of extensive fine-grained siliciclastic rocks along the Laurentian margin (Cecile et al., 1997; Lund, 2008).

Mid-Cambrian to Upper Devonian magmatism is found at a number of stratigraphic levels and has been linked with episodic extension (Cecile et al., 1997; Lund, 2008). Magmatic sill complexes and alkalic volcanism are concentrated along rift-parallel normal faults, and in particular at transfer-transform zones where there is offset between these faults (Goodfellow et al., 1995). This low-volume post-breakup magmatism has been linked to margin-scale extension. The age and chemistry of the volcanic rocks is consistent with a post-breakup origin and low-degree partial melting of an enriched lithospheric mantle source, comparable with hyperextension in a magma-poor continental rift environment (Campbell et al., 2019).

There were three main periods of CD-type metallogenesis during the evolution of the passive continental margin in the Selwyn Basin (Goodfellow, 2007). Deposits are located in fine-grained, carbonaceous units during the Cambrian, Silurian and Devonian, which also coincide with periods of magmatism (Goodfellow et al., 1995). Magmas accumulated at the base of the crust have been proposed as a potential conductive heat source for the hydrothermal activity during mineralization (Goodfellow, 2007). However, despite observations that transfer-transform zones are associated with the distribution of CD-type deposits (Lund, 2008) there is no evidence of direct magmatic input to any of the Selwyn Basin CD-type deposits. Rather, it has been suggested that both low-volume magmatism and hydrothermal activity were mutually exclusive features of the tectonic environment (Magnall et al., 2016). Similar to deep-seated magmatism, crustal extension in magma-poor continental margins can also result in anomalously high geothermal gradients (e.g. 80°C/km; Hart et al., 2017).

For the model geoemetry, a condensed stratigraphy along a 250-km long two-dimensional cross-section was developed from the compilations from Gordey and Anderson (1993) and Martel et al. (2011) (Figure 1), including the Windermere Supergroup (Neoproterozoic: shales, siltstones, sandstones, conglomerates, dolostones and limestones), Hyland Group (Neoproterozoic to Lower Cambrian: shales, siltstones sandstones and conglomerates), Road River Group (Ordovician to Silurian: shales, mudstones and siltstones) and Earn Group (Lower to Upper Devonian: shales, sandstones, conglomerates and limestones). The right-hand side of the modeling domain represents the Mackenzie Platform, which comprises Neoproterozoic to Middle Devonian limestones and dolostones overlain by Upper Devonian siliciclastic units. The Mackenzie Platform and part of the Selwyn Basin on the left-hand side of the domain are underlain by local basement, the Mackenzie Mountains Supergroup (Neoproterozoic: sandstones and dolostones).

The thickness of the sedimentary sequence of the Selwyn Basin increases with distance from the continental margin and can be more than 30 km (Cook et al., 2004). Only the first 10 km are considered in the simulations, because beneath this level, permeability and porosity values are expected to be too low to be significant for the ore-forming hydrothermal system (Garven et al., 2001; Ingebritsen & Manning, 2010). Toward the center of the profile, the rock domains have a gentle slope to the left, representing a typical rift

Figure 1. Simplified geologic map and cross-section across the Selwyn Basin and Mackenzie Platform in Western Canada, with a condensed stratigraphy and the location of clastic-dominant (CD-type) and Mississippi Valley-type (MVT) deposits (Goodfellow, 2007; Gordey & Anderson, 1993; Martel et al., 2011). The stratigraphic column is a condensate of the Selwyn Basin and adjoining McKenzie Platform, with hiatuses represented by vertical lines (modified from Martel et al., 2011). The two-dimensional modeling domain is 250 km wide, but only an area of 50 km width around the three faults above the maximum bottom heat flux (dashed rectangle) is shown in Figures 2–6. Depth is shown relative to the lowermost location of the seafloor on the left-hand side and horizontal distance relative to the maximum bottom heat flux. Note that the vertical scale is exaggerated in the representation of the full domain, but is to scale in the 50 km-excerpt, which also shows the mesh resolution. The temporal evolutions of temperature and metal contents at the modeled deposit site in the uppermost grid cell along the central fault (observation point) are shown in Figure 7.

structure. Three 100-m wide fault zones are included with a dip angle of 45°, representing typical normal faults in extensional sedimentary settings (Jackson, 1987; Morley, 1995). The model is discretized using 73,100 triangular elements with a progressive mesh refinement in the fault domains. The uppermost cells of the mesh represent both the seafloor and the shallow subsurface, so the simulations cannot provide any constraints on the source of reduced sulfur or precise location of mineralization.

3. Methods

3.1. Numerical Model

We calculate fluid flow with a continuum, porous medium approach using the Control Volume Finite Element Method numerical scheme implemented in the Complex Systems Modeling Platform (Weis et al., 2014). The model can represent compressible fluid flow using a realistic representation of nonlinear fluid properties (e.g. density, viscosity, enthalpy) and physical separation of fully miscible, multi-phase fluids (liquid, vapor and halite) in the H_2O-NaCl system, covering temperatures up to 1000°C and pressures up to 500 MPa (Driesner, 2007; Driesner & Heinrich, 2007). We calculate energy and mass conservation by solving for adective fluid flow, thermal conduction as well as diffusion and dispersion of solutes (Bear, 1972; Ingebritsen et al., 2006; Phillips, 1991). We assume that fluid and rock are in local thermal equilibrium, requiring that the total enthalpy is distributed over the fluid and rock contained in a given mesh volume. A detailed description of the numerical approach and benchmark solutions are provided in Weis et al. (2014).

We apply constant permeability values for the simplified stratigraphy according to the predominant lithology in each rock domain (Figure 1). The lowest permeability values are assigned to the quasi-impermeable basement (10^{-19} m^2) and the shale-dominated Road River Group (5.0×10^{-19} m^2), which is the main aquitard within the Selwyn Basin. Intermediate permeability values that allow advective solute transport but inhibit advective heat transport (Ingebritsen et al., 2006) have been assigned to the uppermost layers comprising the shale-containing Earn Group of the Selwyn Basin (10^{-17} m^2) and the Mackenzie Platform (10^{-16} m^2). At the base of the sequence, the sandstones and conglomerates of the Windermere Supergroup that are assumed to form a potential aquifer and metal source rock have been assigned a permeability value typical for advective heat transfer (10^{-15} m^2). The Hyland Group, which contains both abundant shale and sandstone layers, has been modeled both as an aquitard (5.0×10^{-19} m^2) and aquifer (5.0×10^{-15} m^2). When inactive, fault zone domains are given the same permeability values as their host units. With faulting, these fault zone domains are assigned the highest permeability values in the modeling domain (10^{-14} m^2). Constraints from steady-state models and in-situ measurements from continental margins worldwide consistently indicate temporally and spatially averaged fault zone permeabilities in the range of 10^{-13}–10^{-15} m^2 (Saffer, 2015). We assume that permeability at several kilometers depth is dominantly generated by microfracturing and therefore use isotropic values.

Bathymetry-dependent constant hydrostatic fluid pressures (2.87–9.85 MPa) are used to describe the top boundary of the modeling domain, which represents the seafloor at depths from 300 m (right side) to 1,000 m (left side) below sea level. The temperature at the top can vary between a constant value of 10°C on nodes with fluid recharge and variable values at discharge nodes, allowing for high-temperature venting. A constant seawater salinity of 3.2 wt. % NaCl is used for the initial and recharge fluids. The bottom boundary at about 10-km depth is treated as impermeable and uses a background heat flux (75 mW/m^2), in agreement with measurements in the northern Canadian Cordillera (Hyndman, 2010; Lewis et al., 2003). As a heat anomaly to drive fluid flow, the introduction of a bell-shaped heat flux is centered at 85 km (below the central fault) and follows a Gaussian profile ($Q_{min} = 75$ mW/m^2, $Q_{max} = 150$ mW/m^2, $\sigma = 10$), consistent with a low-viscosity crustal layer due to partial melting and/or hydration within a continental crust during active extension (Li et al., 2019). The left and right boundaries use no-flow conditions and have been placed far away from the domain of interest to avoid boundary effects.

We use constant and uniform values for rock density (2,400 kg m^{-3}), porosity (10%), heat capacity (880 J kg^{-1}°C^{-1}), thermal conductivity (2.5 W m^{-1}°C^{-1}), and diffusion-dispersion coefficients (10^{-12} m^2 s^{-1}).

3.2. Proxies for Metal Leaching and Enrichment

The main focus of this study is on the physical hydrology and thermal evolution of the basin during an idealized ore-forming event. Advective fluid flow at temperatures above 300°C is of critical importance, because metal solubilities in hydrothermal fluids are strongly temperature dependent. Metal leaching, transport and precipitation in nature depends on chemical speciation and therefore also on other parameters like pH and redox conditions. However, full reactive-transport modeling rather focusses on lower-temperature and geochemically less complex systems (Yao & Demicco, 1997; Yapparova et al., 2017a, 2017b) and the thermodynamic databases that can cover chemical speciation for base metal transport at such high temperatures are currently still under development, e.g. investigating the roles of chloride and bisulfide complexing for metal transport (Etschmann et al., 2019; Zhong et al., 2015). Therefore, numerical simulations of high-temperature hydrothermal systems commonly single out the strong temperature dependence of metal solubility to constrain their potential to form ore deposits, such as porphyry copper or volcanic-hosted massive sulphide deposits (Andersen et al., 2017; Weis et al., 2012).

As a simplification, this study focusses on the thermal controls on metal leaching and enrichment by introducing proxies for "metal enrichment potentials", which are calculated using temperature-dependent functions for both Zn and Pb solubilities (log Zn (ppm) = 5.5759–1790.1/T(K); log Pb (ppm) = 4.6716–1338.0/T(K)) in saline fluids from the literature (from Yardley, 2005 and references therein) (Figure S1). Such data are also used for comparison with predictions from thermodynamic models (Zhong et al., 2015) and hence can serve as first-order approximations since there are no adequate modeling tools to predict the redox state, pH and chemical speciation of base metals for multi-phase fluid flow at the temperature range of interest for this study. Uniform Zn and Pb concentrations (128 and 23 ppm, respectively) have been used for the initial rock conditions over the entire modeling domain, and are based on average values from leaching experiments on samples from drilling along a transect across western Canada (Lydon, 2015).

In our numerical model, the initial concentrations of Zn and Pb in the sedimentary units can be leached, transported and precipitated by the hydrothermal fluids during the evolution of the simulated hydrothermal system. Slow fluid flow velocities provide the justification for assuming that fluids undersaturated in Pb and Zn can efficiently leach these metals from the host rock in the given mesh volume until full depletion. Fluids then become oversaturated and precipitate Zn and Pb due to temperature changes during fluid transport. Remobilization and reprecipitation of metals can also occur during subsequent fluid flow but fluids leaving the modeling domain to the ocean precipitate all their metal contents at the top boundary, mimicking the formation of massive sulphide deposits at or near vent sites. We then calculate Zn and Pb enrichment potentials by dividing the simulated Zn and Pb contents of rock and fluid at a given timestep by their respective initial contents, with values between 0 and 1 indicating regions of net metal leaching and values above 1 providing the local enrichment factor with respect to the metal content of average sedimentary rocks. Economic ore grades in sediment-hosted base metal deposits typically require enrichment factors of at least 1000 (Heinrich & Candela, 2014; Wilkinson, 2014). For the hypothetical ore deposit at the observation point (Figure 1), we then calculate a potential metal endowment in Mt for comparison of our modeled proxy with the real deposits.

3.3. Assumptions, Limitations and Scope

The simplified, generic modeling set-up relies on a number of assumptions that should be considered for the following discussion. We model a potential ore-forming period in the Late Devonian, but sedimentary basins develop over much longer time spans in response to geodynamic processes and so do the fluids retained in, and passing through, their rock units. The model is also restricted to a two-dimensional cross-section of a nominal thickness of 1 m in the 3rd dimension. Leaching, precipitation and remobilization of metals in the subsurface will likely be less efficient than modeled here and will be a function of chemical speciation (incl. pH, redox). Also, the model does not account for salinity-dependent solubility of metals, but rather investigates the potential to form a deposit from hydrothermal circulation of fluids that originated from normal seawater.

With increasing depth, the absolute permeability values of sedimentary layers will be less dependent on intergranular pore space and controlled more by fracture networks, which can greatly vary within tectonically

Table 1
Simulation Set-Ups

Simulation	Figures	Scenario parameters			
		Timing of fault opening (Myr)	Initial pressure	Permeability of Hyland Group	Timing of heat anomaly (Myr)
1	2, 6a, 7a	0.5	hydrostatic	aquitard	0
2	3, 6b, 7a	0	hydrostatic	aquitard	0
3	4, 6c, 7a	0	lithostatic	aquitard	0
4	7a	0.5	lithostatic	aquitard	0
5	7a	1	lithostatic	aquitard	0
6	5, 6d, 7b	0	lithostatic	aquifer	0
7	7b	0.5	lithostatic	aquifer	0
8	7b	1	lithostatic	aquifer	0
9	7c	1.5	lithostatic	aquitard	1
10	7c	1.5	lithostatic	aquifer	1

active crust (Ingebritsen & Manning, 2010). There may be time periods with purely conductive heat transfer and suppressed fluid flow. This can be modeled by calculating initial temperature conditions that follow a linear geothermal gradient calculated from the applied bottom heat flux (including or excluding a heat anomaly). Initial fluid pressures are calculated assuming either a hydrostatic or lithostatic pressure gradient as end-member scenarios, depending on the assumed pore-space connectivity within the sedimentary units at depth. During tectonically active time periods of basin evolution, the permeability of deep sedimentary units and fault zones can then be increased due to stress-related microfracturing and fault activation, respectively, leading to basin-scale fluid flow.

The numerical model aims to simulate the hydro-geochemical response to a rifting event during extension and thinning of the continental crust. In a series of simulations (Table 1) different parameters are varied to evaluate (1) the timing of fault opening (at simulation times $t = 0, 0.5, 1.0$ and 1.5 Myr), (2) the initial fluid pressure distribution from hydrostatic (free convection) to lithostatic (overpressured, confined), (3) the permeability of the Hyland Group (aquitard vs. aquifer), and (4) the timing of the heat anomaly (at simulation times $t = 0$ and 1 Myr).

4. Results

4.1. Fluid Evolution

The initial geothermal gradient results in a temperature distribution with a bulge above the heat anomaly described by the bell-shaped bottom heat flux profile (Figure 1). The units with relatively low permeability values (basement and Earn, Road River and Hyland Groups) have a conduction-dominated temperature profile (Figure 2a, simulation 1). In contrast, heat transfer within the more permeable Windermere Supergroup as the main aquifer is dominated by fluid advection, resulting in temperature distributions with hotter up-flow and colder down-flow zones. The hydrothermal system starts with several convection cells (e.g. after 100 kyrs; Figure 2a) and Darcy velocities in the order of 10^{-9}-10^{-8} m s^{-1} in the upflow zone, until eventually forming elongated convection cells (500 kyrs; Figure 2b). The part of the Windemere Group at temperatures above 300°C is limited to 10–15 km distance from the peak of the heat anomaly.

Following the opening of the faults after 500 kyr, fluids ascend along the central fault above the peak of the heat anomaly with Darcy velocities of 1–2 orders of magnitude higher (10^{-7} m s^{-1}) and recharge is focused along the two lateral faults with lower fluid velocities compared to the upflow zone (Figure 2c). These structurally and topographically controlled discharge and recharge patterns start to influence the large-scale convective regime within the deep aquifer by reorganization of the original convection cells into cells spanning from fault to fault. After 585 kyrs, the system reaches the highest venting temperatures with 275°C at the tip of the central fault. However, at that time, the deep reservoir above the heat anomaly has already been cooled down due to the incoming colder recharge fluids from the lateral fault zones. This cooling effect continues with time until only a small region between the peak heat anomaly and the fault intersection at the contact between the aquifer and aquitard reaches temperatures above 300°C (1 Myr; Figure 2d). As a result of the cooling, the mobility of the fluids and the buoyancy force for fluid flow are also reduced, leading to a general reduction in fluid velocities. With time, the main upflow zone has moved up the slope of the aquifer from left of the peak anomaly (Figure 2b), to immediately above it (Figure 2c) and finally 2–3 km to the right of it (Figure 2d).

4.2. Timing of Fault Opening

When the faults and the aquifer are activated simultaneously at the beginning of the simulation, hot fluids with temperatures initially up to >500°C can be tapped and transported upward along the central fault (Figure 3, simulation 2). The hydrothermal system develops from a conduction-dominated thermal profile after
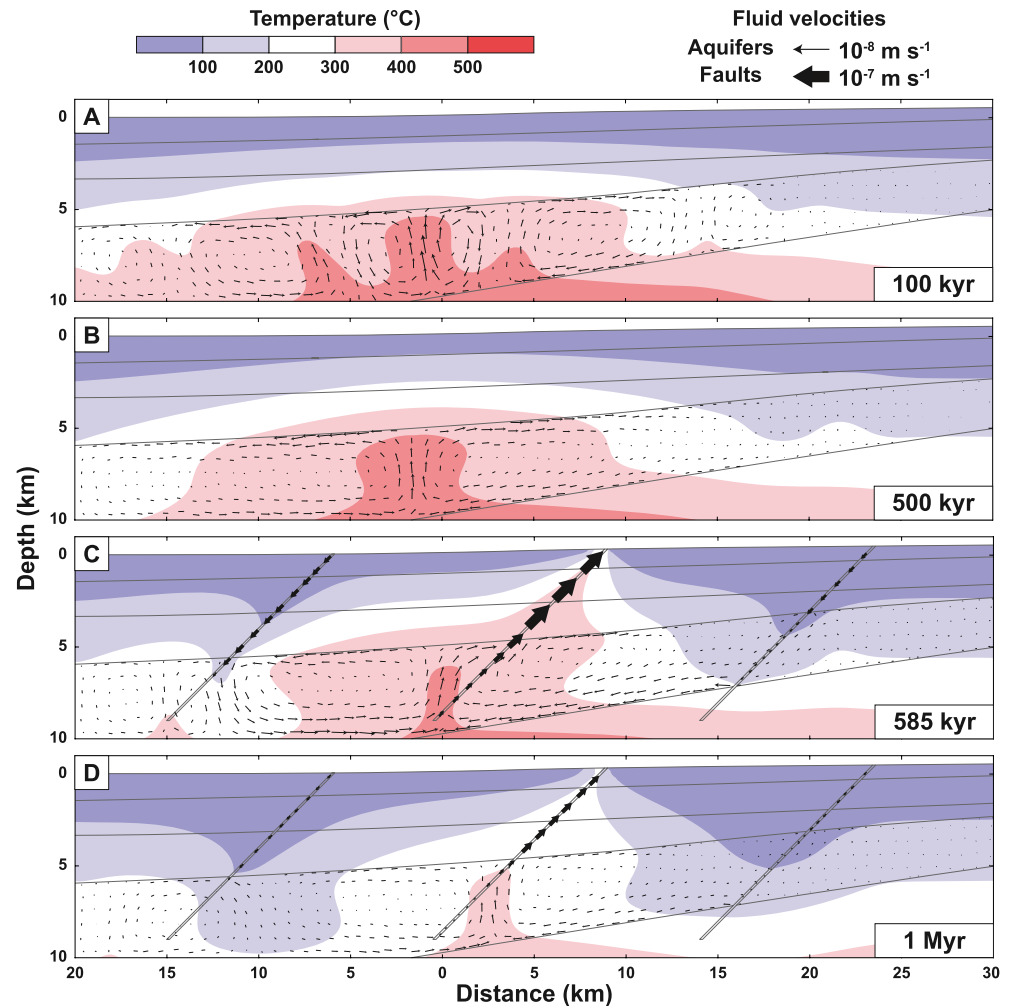
Figure 2. Fluid evolution of the hydrothermal system with the Windermere Supergroup as the main aquifer after 100 kyr (a), 500 kyr (b), 585 kyr (c) and 1 Myr (d) of simulation time with fault activation after 500 kyr (simulation 1, Table 1). The colors show isotherms every 100°C. Fluid velocities use different scales and arrows for flow in aquifers and fault zones and only a selection of arrows are shown for graphical reasons.

1 kyr of simulation time (Figure 3a) to several convection cells after 32 kyr (Figure 3b) and eventually to the large-scale convection pattern in the Windermere Supergroup after 91 kyr (Figure 3c), which is comparable to the state of the hydrothermal system at 585 kyr in the previous simulation (Figure 2c). The hydrothermal system reaches its peak venting temperatures slightly later than the previous simulation (91 kyr compared to 85 kyr after fault opening), but reaches slightly higher temperatures of 282°C. At these peak conditions, the fluids are phase-separating into liquid and vapor, albeit only locally at the vent site.

As in the previous scenario, fluids discharge along the central fault zone and recharge both along the lateral faults, which also leads to continuous cooling of the reservoir. However, the hydrothermal system in simulation 2 is generally hotter than in simulation 1, which experienced 500 kyr of cooling due to heat advection in the deep aquifer prior to fault opening. The generally higher temperatures are also reflected by systematically higher fluid velocities in simulation 2 compared to simulation 1.

4.3. The Role of Fluid Overpressure

When fault opening is started at the beginning of a simulation with a confined, over-pressured reservoir under near-lithostatic fluid pressures, fluids quickly migrate up the continental slope and along all three fault structures (Figure 4a, simulation 3). Fluid velocities reach peak values of about 10^{-8} m s^{-1} within
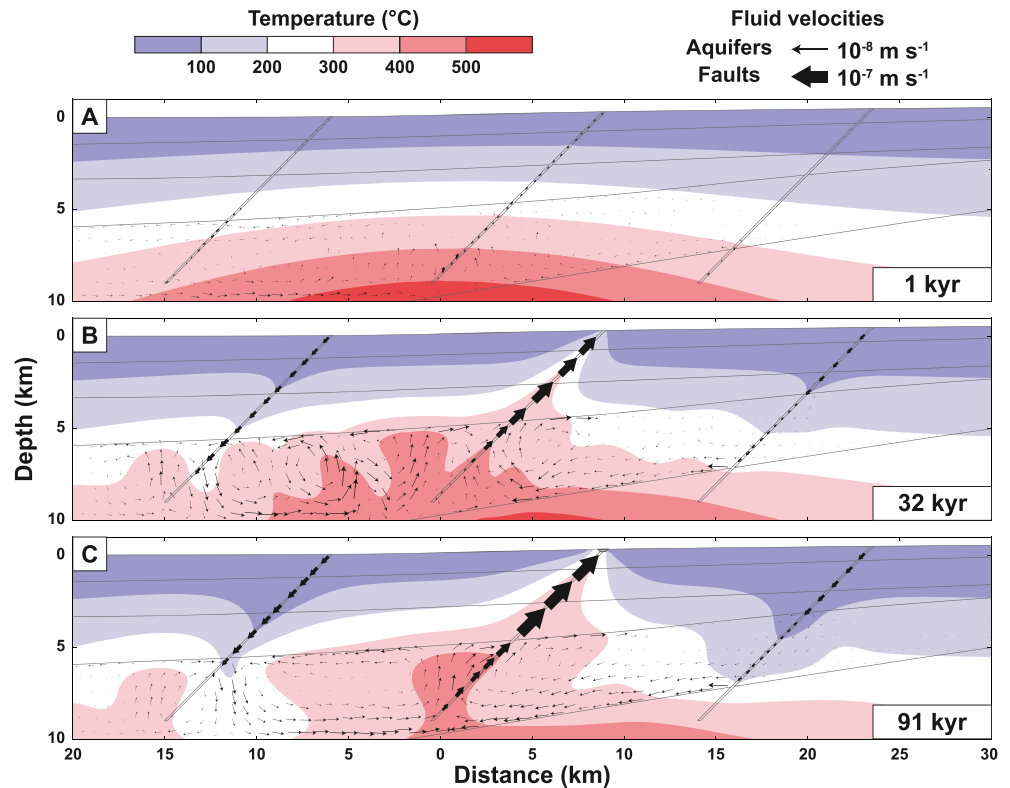
Figure 3. Fluid evolution of the hydrothermal system with the Windermere Supergroup as the main aquifer after 1 kyr (a), 32 kyr (b), and 91 kyr (c) of simulation time with fault activation at the beginning (simulation 2, Table 1). Legend as in Figure 2. The small greenish area at the tip of the central fault indicates two-phase conditions (liquid and vapor).

the aquifer and $2 \cdot 10^{-7}$ m s^{-1} along the left and center fault zones. When fluid pressures are reduced to near-hydrostatic values, up-flow remains focused along the central fault and down-flow is directed along the topographic gradient toward the Selwyn Basin and also along the two lateral faults (Figure 4b). Similar to simulation 2 (Figure 3), the hydrothermal system starts to form convection cells, which eventually result in the same elongated fault-to-fault convection pattern (Figure 4c).

In contrast to the previous two simulations, the hydrothermal system reaches three stages of peak temperature conditions at the vent site of the central fault: an immediate high-temperature pulse with 154°C after 1 kyr (Figure 4a), a second peak with 259°C after 32 kyrs (Figure 4b) and a third peak with 282°C after 91 kyr (Figure 4c). The third peak is identical to the peak with two-phase conditions from the previous simulation without overpressured initial conditions (Figure 3c) and therefore related to the fault-to-fault convection pattern. In contrast, the first two peaks are absent in the previous simulation and have to be related to the initial expulsion phase. While the first peak can be seen as an immediate response of the expulsion event (Figure 4a), the second peak likely represents the arrival time of the hottest fluids from the deep aquifer (Figure 4b). Dividing the maximum depth of the domain (10 km) by the arrival time (32 kyr) gives an average fluid velocity in the order of 10^{-8} m s^{-1} (=0.31536 m yr^{-1}), which is in line with the average velocities calculated for the system. The initially expelled fluids with a temperature of >500 °C are cooled during ascent by admixing of cooler fluids from shallower levels of the aquifer after fluid pressures drop to near-hydrostatic values and by conductive heat loss to the sides of the fault zone, eventually reaching the venting temperature of 259°C at 32 kyrs.

In comparison to the simulation without initially overpressured conditions, the hydrothermal system from the simulation with overpressure is notably cooler both after 32 kyrs (Figures 3b and 4b) and 91 kyrs (Figures 3c and 4c), indicating that the initial fluid expulsion phase increased the rate of heat transfer from deeper to shallower levels.
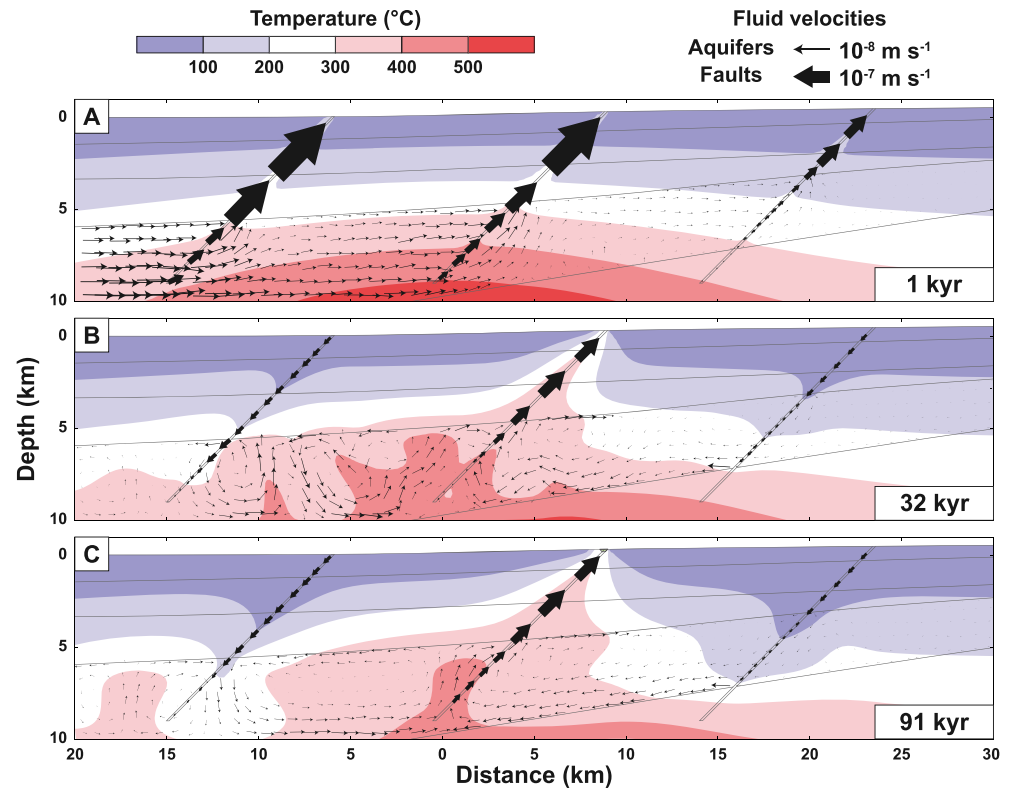
Figure 4. Fluid evolution of the hydrothermal system with the Windermere Supergroup as the main aquifer after 1 kyr (a), 32 kyr (b), and 91 kyr (c) of simulation time with fault activation at the beginning and an initially overpressured reservoir (simulation 3, Table 1). Legend as in Figure 3.

4.4. The Role of Strata Permeability

When the Hyland Group is treated as an additional aquifer, fluid flow velocities during the initial expulsion stage are similar to the ones of the previous simulation in the uppermost parts of the fault zones, but are reduced in the Windermere Supergroup (Figure 5a). Velocities within the Hyland Group are similar to the ones within the Windermere Supergroup in the simulations with the Hyland Group as an aquitard (Figures 4a and 4b).

After the initial expulsion phase and during large-scale convection, fluid velocities in the Windemere Supergroup are similar to the ones in previous simulations (Figures 5b and 5c). Deep convection is connected to fluid flow in the Hyland Group at intermediate depth, where fluid velocities are increased to values up to several 10^{-8} m s^{-1}, due to the higher strata permeability (Figure 5b). While the velocities of fluid recharge are similar to the ones of the previous simulation, the fluid velocities along the central fault zone are reduced (Figures 4b and 5b). The vertically more extended convective pattern results in faster cooling of the basin. For example, at 32 kyrs the Windemere Supergroup has cooled almost entirely below 400°C (Figure 5b), in contrast to the simulation with the Hyland Group as an aquitard (Figure 4b).

After 161 kyrs, the system has cooled further and fluid advection has established the fault-to-fault convection pattern between both aquifers (Figure 5c). Fluid velocities in the fault zones are considerably reduced. Fluid velocities in the aquifer are highest in the vertical up-flow zone and in the horizontal flow at the contact to the overlying low-permeability units of the Road River Group.

As in the previous simulation with an initially overpressured reservoir, the system develops three high-temperature events. The first temperature peak of 139°C is after 1 kyrs (Figure 5a). The second temperature peak of 242°C is after 32 kyrs and represents the arrival of the hottest fluids at the central fault zone (Figure 5b). Both of these temperatures are lower than in the simulation with the Hyland Group as an aquitard, reflecting the additional cooling by advective fluid flow at intermediate depths. The third peak arrives after
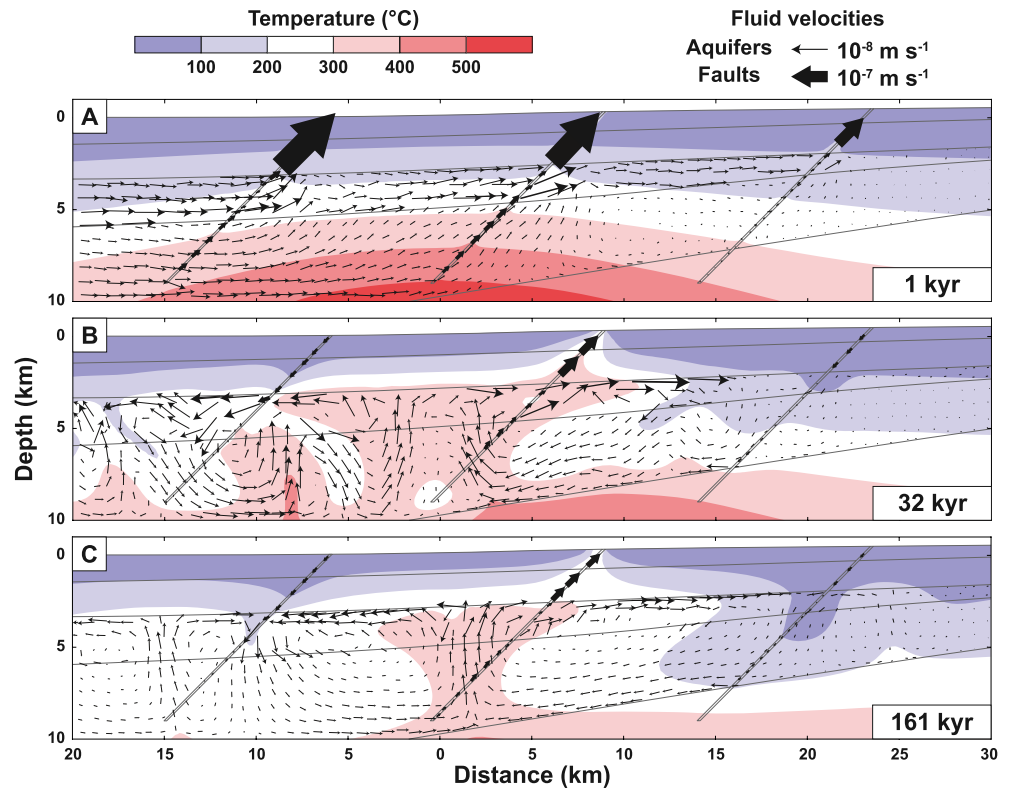
Figure 5. Fluid evolution of the hydrothermal system with the Windermere Supergroup and Hyland Group as the main aquifers after 1 kyr (a), 32 kyr (b), and 161 kyr (c) of simulation time with fault activation at the beginning and an initially overpressured reservoir (simulation 6, Table 1). Legend as in Figure 2.

161 kyrs (Figure 5c), which is considerably later than in the previous two simulations. The maximum vent temperature of 224°C resulting from the fault-to-fault convection pattern is also considerably lower than in all previous simulations, and this time is even lower than the second peak.

4.5. Metal Leaching and Enrichment

The temperature-dependence of metal solubility leads to efficient metal leaching at temperatures exceeding 300–350°C (red areas in Figures 2–5) and metal accumulation in regions where fluid flow is cooled below this temperature threshold (white areas in Figures 2–5). Areas with temperatures below 200°C (blue areas in Figures 2–5) and low permeabilities remain essentially unaffected by advective metal transport. Figure 6 shows the degree of zinc leaching (with >50% and >90% of depletion represented by light and dark blue areas, respectively) and enrichment (with factors >2, >10 and >100 represented by green, yellow and red areas, respectively) at time steps 500 kyr after fault opening for the four simulations (Figures 2–5) as calculated from our proxy using temperature-dependent metal solubilies.

The results show that hydrothermal convection within the aquifers above the heat anomaly is very efficient in leaching (almost) all of the metal content. However, at the contact with the overlying aquitard, i.e. the Hyland Group (simulations 1–3; Figures 6a–6c) or the Road River Group (simulation 6; Figure 6d), where the hydrothermal flow system cools, metals are concentrated in two distal regions located at the down-flow limbs of the convection patterns (between 10 and 20 km from the heat anomaly). This metal enrichment encompasses a large section up the slope of the sedimentary sequence toward the Mackenzie Platform. In all simulations, this is the region where the circulating fluids are cooled most efficiently both from recharge fluids descending along the right fault zone and along the topography of the aquifer. During continuous cooling of the basin, metal solubilities remain too low for remobilization. With enrichment factors below 100, these areas of metal accumulation would be uneconomic, but they cover relatively large areas and
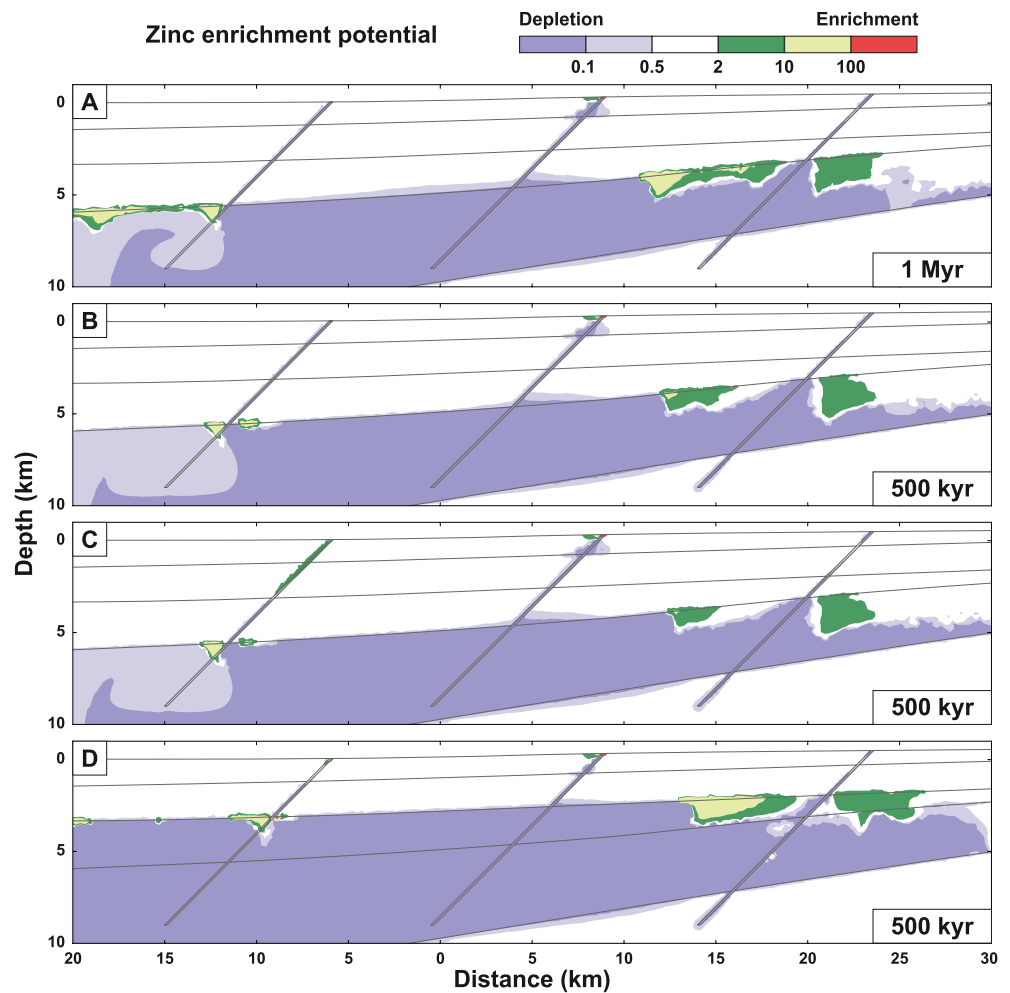
Figure 6. Zinc enrichment potential 500 kyr after fault opening in simulation 1 (a), 2 (b), 3 (c) and 6 (d), calculated as the ratio between total zinc content in fluid and rock divided by the initial zinc content. Leached regions are shown in blue (depletion <0.5) and different degrees of enrichment are shown as green, yellow and red areas.

hence reduce the total amount of metals available for ore formation at the main up-flow zone along the central fault. Simulations 1 and 6 (Figures 6a and 6d) show a higher degree of enrichment than simulations 2 and 3 (Figures 6b and 6c).

Metal accumulation due to cooling can also be observed where the left fault zone intersects the top of the main permeable aquifer (Windemere Supergroup in Figures 6a–6c and Hyland Group in Figure 6d). In simulation 1, an area with more than a 10-fold zinc enrichment stretches along several kilometers to the left side of the left fault zone (Figure 6a). In the three other simulations, this enrichment zone is more localized and also appears at the right side of the fault zone (Figures 6b–6d). In simulation 3 and to a lesser degree in simulation 6, there is an additional minor >2-fold enrichment along the upper parts of the left and right fault zones (Figure 6c, green areas). These minor metal accumulations result from the initial expulsion phase of deep fluids from the overpressured reservoir. After flow reversal from discharge to recharge, fluid temperatures are too low to efficiently remobilize these metals, and hence, they also slightly reduce the total amount of zinc available for ore formation. In simulation 6, the zinc enrichment potential locally reaches values above 100 (small red region in Figure 6d), where the horizontal flow of >200°C hot fluids at the contact of the high-permeability Hyland Group and the low-permeability Road River Group is sharply cooled to below 200°C by the recharging fluids from the left fault zone (Figure 5c).

The highest values of zinc enrichment potential are reached at the uppermost segment of the central fault zone. Some minor accumulation (>2-fold enrichment) spreads out laterally, but most of the zinc is
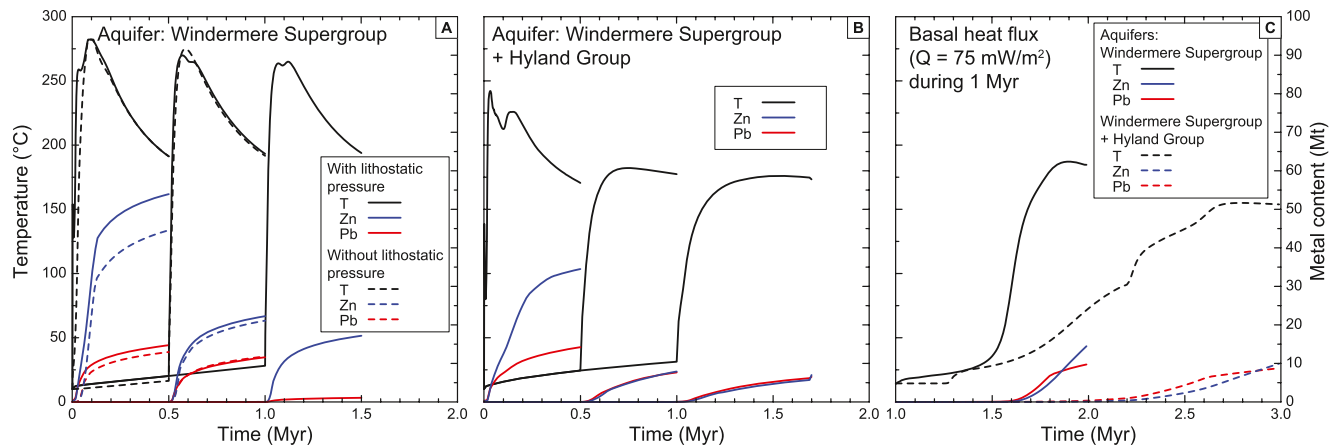
Figure 7. Temporal evolution of temperature and metal content (Zn and Pb) at the modeled deposit site at the uppermost grid cell along the central fault (circle in cross-section of Figure 1) from model scenarios using the Windermere Supergroup as the main aquifer (a, simulations 1–5), the Hyland Group as an additional aquifer (b, simulations 6–8), and applying a constant basal heat flux prior to the onset of the bell-shaped heat anomaly at 1 Myr and fault opening at 1.5 Myr (c, simulations 9 and 10).

accumulated at one location with enrichment values exceeding 10,000 (small red region at the tip of the central fault in Figures 6a–6d). Even though the fluids are cooled during their ascent from the deep aquifer, all the zinc content is eventually transported up to the uppermost cells near the vent site, while the rest of the fault zone shows an almost complete depletion (values of <0.1; dark blue). This depletion within the entire fault zone documents that, with time, the hot fluids ascending along the central fault zone from the deep aquifer have become undersaturated in metals, because the remaining metal contents in the deep aquifer have been redistributed to lower-temperature regions where they are not efficiently remobilized, which lowers the potential of the system for further metal enrichment.

The results of lead enrichment potential show the same general features (Figure S2), although there are some deviations from the zinc enrichment potential that relate to the difference in temperature dependency and the lower initial concentrations in the host rock. Additional simulations with increased diffusion-dispersion coefficients of 10^{-8} m^2 s^{-1} show some additional metal leaching from low-permeability units (Figure S3). However, the effect on the locations and amounts of metal enrichment is relatively minor, confirming that advective fluid flow is the key first-order process for ore formation in these systems.

4.6. Constraints on Ore Formation

The highest temperatures and metal enrichments at the modeled site of ore formation are produced with near-lithostatic fluid pressures in the initial conditions and when fault opening is simultaneous with the heat anomaly at the beginning of the simulation (simulation 3; Figure 7a). The temperature during the transient expulsion event reaches 259°C in the initial phase of 32 kyr, followed by a peak of 282°C after 90 kyr, the latter temperature being controlled by two-phase conditions. This temperature is identical to the simulation with initially hydrostatic fluid pressures (simulation 1), indicating that through-going convection across a deep aquifer is essential to reach high venting temperatures. Fault opening in the simulations at later times (0.5 and 1.0 Myr; simulations 4 and 5) produces a slight decrease in maximum temperature values (270 and 264°C, respectively) and arrival times after fault opening (72 and 69 kyr, respectively).

The timing of fault opening and fluid overpressure conditions has even stronger effects on the maximum Zn and Pb contents than on the temperature evolution. The initial mobilization phase from an overpressured reservoir results in metal enrichments of 45 Mt Zn and 10 Mt Pb. After this initial phase, metal concentrations increase with time without reaching stable values, suggesting that the maximum metal contents are also dependent on the timing of fault closure and, therefore, related to the duration of the rifting event. The Zn contents are reduced when the reservoir is not overpressured during activation and the initialization phase reaches a value of~35 Mt Zn. Fault opening at later stages of the simulation results in significantly less metal endowment even though the peak temperatures are still above 250°C. The reduction in

maximum metal contents corresponds with the previously described mechanism of metal accumulation in regions where colder recharge inhibits remobilization (Figure 7a, simulations 1–5).

With the Hyland Group as an aquifer, the arrival times of the maximum venting temperatures after fault opening increase from 32 to 260 and 560 kyr and temperatures decrease from 242 to 182 and 176°C (Figure 7b; simulations 6–8). Despite the total mass of extractable metals in the potential permeable source rocks being larger, the total metal endowments at the simulated ore deposit site are significantly lower for Zn (the effect is less pronounced for Pb and with time).

Simulations were also performed to evaluate fluid convection with a constant background heat flux of 75 mW/m^2 followed by the introduction of the heat anomaly after 1 Myr and fault opening after 1.5 Myr (simulations 9 and 10; Figure 7c). These scenarios result in low venting temperatures and ore grades. With the Hyland Group as an aquitard, maximum venting temperatures of 187°C and metal enrichment of 10 Mt Zn and 9 Mt Pb are observed 0.9 Myr after the faults are opened. With the Hyland Group as an aquifer, maximum venting temperatures of 155°C and metal contents of Mt Zn and 8 Mt Pb are reached 1.79 Myr after fault opening.

5. Discussion

5.1. Heat Anomaly and Stratigraphic Confinement

The modeling results show that convective hydrothermal flow in the aquifers before fault opening suppressed the temperature and overall metal budget of the mineralizing fluids. This effect is even more pronounced if fluid circulation with a basal heat flux preceded the bell-shaped heat flux. Rather, the most efficient ore-forming system develops when a heat anomaly is introduced to a conduction-dominated basin with confined sedimentary layers, which inhibit fluid advection during this pre-heating phase. The assumption of a conduction-dominated regime infers that the permeability values of even the coarser clastic units were relatively low when reaching several km burial depth, which is consistent with depth-dependent permeability profiles (Ingebritsen & Manning, 2010).

Such high geothermal gradients, like the one used in the models, could reflect either deep-seated magmatism or crustal extension in magma-poor continental margins (Hart et al., 2017). It was recently proposed that the Cordilleran margin of NW-America formed as a result of protracted (>300 Myr) hyperextension of continental crust during magma-poor rifting, analogous to the Newfoundland–Iberian rift system (Beranek, 2017; Campbell et al., 2019). In the Nahanni district that borders Macmillan Pass, a mixture of turbiditic silt- and mudstones from the Hyland Group overlies the thick sequences of the syn-rift lithologies of the Windermere Supergroup (Gordey & Anderson, 1993). It is possible, therefore, that stratigraphic confinement of the Windermere Supergroup by these fine-grained sedimentary rocks resulted in the retention of heat deep in the basin. The optimal conditions then involve the Hyland Group acting as an aquitard and thermal insulator to the underlying Windermere Supergroup, which was the main source package for the metals. The generation and maintenance of fluid pressures above the hydrostatic gradient require the presence of a low-permeability barrier along the upper boundary of the overpressured region (Hunt, 1990; Powley, 1990). Extended periods with conduction-dominated thermal profiles and suppressed fluid flow in the sedimentary basin would provide the heat and time for the pore fluids to leach the metal contents from the source rocks.

5.2. Episodic Rifting and Ore-Forming Events

In hyperextended settings, extension is typically accommodated by brittle behavior that is focused along faults (Pérez-Gussinyé et al., 2001). Metallogenesis in the Selwyn Basin post-dated the main stage of continental rifting, although the location of CD-type deposits in the Selwyn Basin has been linked to the reactivation of earlier rift structures during short-lived extensional episodes in the Late Cambrian, Early Silurian, and Late Devonian (Lund, 2008). Periodic extension likely resulted in transient permeability pathways for fluids from the deep, confined aquifer to reach the shallow subsurface and the sites of CD-type mineralization. Indeed, the most efficient way to form a Zn-Pb deposit in the numerical simulations is to breach the hot, overpressured fluid reservoir of the Windermere Supergroup. However, if the aquifer permeability

is increased prior to fault opening, metals can be mobilized by fluid flow in the aquifer and accumulate in lower-temperature domains in the basin, where they are not remobilized by later recharge fluids.

The role of faults in providing a conduit for fluids sourced from depth is a feature of sedimentary basins, and even for relatively low displacement faults (<200 m) it is possible that these permeability structures extend deep into the underlying basement and even the mantle (Davidheiser-Kroll et al., 2014; Muchez et al., 2005; Walsh et al., 2018). The permeability of faults tends to be a transient and heterogeneous parameter (Bekins et al., 1995; Neuzil, 2019; Saffer, 2015) that can be enhanced or decreased in response to tectonism, fluid production and geochemical reactions (Ingebritsen & Gleeson, 2015; Manga et al., 2012). Episodic flow regimes in which fault ruptures tap into overpressured fluid reservoirs have been described qualitatively as fault-valve models (Cox, 1995; Sibson et al., 1988). Fault-valve processes result in episodic migration of fluid batches through fault-controlled hydrothermal systems (Cox, 2005). Nevertheless, an increase of fault zone permeability alone would lead to locally restricted hydrothermal convection and greatly reduce the volume of source rock that can be leached. Our modeling results suggest that simultaneous permeability increases in both faults and aquifers are required to maximize the ore-forming potential of the hydrothermal system.

Our results indicate that short-lived mineralization events in the order of 100 kyr related to a basin-scale extensional event have the greatest potential to form high-grade fault-controlled ore deposits. Assuming similar processes, Cathles & Smith (1983) predicted that overpressured fluids in sedimentary basins could be expelled into overlaying strata and events shorter than 1 kyr every 1 Myr could explain mineral zonation patterns and temperatures recorded in MVT deposits. Numerical models by Ranganathan & Hanor (1989) and Ranganathan (1992) demonstrate that the expulsion of overpressured fluids along the Welsh salt dome in southwestern Louisiana formed brine plumes with a duration of less than 10 kyr. Additionally, numerical simulations of fluid flow and heat transport in the South Eugene Island minibasin, offshore Louisiana, show that expulsion of overpressured fluids along faults can produce temperature and pressure anomalies within a short time (250 yr) after fault opening (Roberts et al., 1996).

Despite the limitations of our modeling approach (see Methods), the calculated metal contents are within one or two orders of magnitude of the values reported for the CD-type deposits in the Selwyn Basin of Zn (2–6 Mt) and Pb (1–2 Mt) (Goodfellow, 2007), indicating that the modeled hydrothermal systems represent first-order processes on the appropriate scale. The timescale is in general agreement with other numerical modeling results (Cathles & Adams, 2005; Garven et al., 2001; Yang et al., 2004, 2006) and supported by recent deposit-scale studies, which have suggested that mineralization could form on short timescales via sub-seafloor replacement processes (Magnall et al., 2020). The simulations indicate that the predicted ore grades keep increasing slightly as long as the fault structures are open (Figure 7). However, rather than the long syn-depositional timescales invoked by SEDEX processes, these results mean that the formation of stratabound sulphide mineralization in the subsurface will be more dependent on the magnitude of fluid input and efficiency of fluid-rock interaction.

5.3. Implications

Previous studies on CD-type deposits have emphasized the role of high-salinity brines for enhancing base metal solubilities and strongly reducing conditions at the seafloor as a metal trap. Both of these pre-requisites require specific oceanographic, geochemical and hydrological conditions. In contrast, our modeling results indicate that it is possible to produce high grades using standard seawater-salinity fluids in a continental margin setting, given the right thermal architecture and timing of extension events. Our results contrast with recent work that has suggested that the suppression of geothermal gradients and fluid temperatures (<250°C) are important geodynamic factors for the metallogenesis of sediment-hosted ore deposits (Hoggard et al., 2020). Such conclusions may be relevant for McArthur-type deposits, but we would argue that heat enhances metal solubility in lower-salinity fluids, which may be more typical of Selwyn-type deposits. Where a fault provides a permeability structure to the shallow subsurface, fluid cooling and the presence of reduced sulfur in the shallow subsurface then results in metal deposition (Magnall et al., 2020).

Altogether, the results indicate that basin geometry and the location and timing of fault zones and heat input control the ore-forming potential at certain areas of the basin. Magma-poor hyperextended continental margins may provide ideal alignments of fault geometries, lithological units, heat input and topographic

effects to increase the ore-forming potential. In the Selwyn Basin, the metal source was likely associated with the earlier stages of basin evolution. Rodinian breakup and the formation of the Laurentian margin coincided with Snowball Earth deglaciation and resulted in the deposition of a thick sequence of immature syn-rift clastic sedimentary rocks (Brenhin Keller et al., 2019). Leaching of metals from the Windermere Supergroup would have been particularly efficient under elevated geothermal gradients that were associated with crustal hyperextension. The Windermere Supergroup was then likely insulated by a thick sequence of fine-grained sag-phase siliciclastic rocks that served as an aquitard and thermal blanket, thereby ensuring the development of a heated, confined aquifer.

6. Conclusions

We used numerical fluid flow modeling to assess the hydro-geochemical response to an extensional tectonic event at a passive continental margin and the formation of clastic-dominant (CD-type) massive sulfide deposits, taking observations from the Selwyn Basin in Canada as geological constraints for the model. We varied the timing of fault opening, the initial pressure distribution (overpressured vs. free convection), the permeability within the stratigraphic sequence (aquifer vs. aquitard), and the heat input. Tapping hot, overpressured, metal-rich fluids from a permeable and confined aquifer at 3–10 km depths and rapid migration along fault structures to the shallow subsurface present the most favorable conditions for the formation of Zn-Pb ores within a hyperextended margin. Extending the aquifer to shallower depths lowers the efficiency of ore formation, even though it increases the total mass of metals in potential permeable source rocks. Hydrothermal convection within the source rocks of the aquifer prior to fault opening reduces the ore-formation capacity because it leads to cooling and thereby the reduction of metal solubility in the fluids. On the other hand, hydrothermal convection through the aquifer after a fluid expulsion event is required for sufficient mass flux of high-temperature metal-rich fluids to make an economic deposit. The later the opening occurs after the heating event, the lower are the temperatures and metal contents of the mineralizing fluids. The time frame to create a Zn-Pb ore deposit similar to the ones in the Selwyn Basin is between 90 kyr and 1.79 Myr, with shorter-lived events producing higher ore grades.

Data Availability Statement

The study uses the software CSMP++ and the algebraic multi-grid solver SAMG, which are subject to licensing via https://mineralsystems.ethz.ch/software/csmp.html and https://www.scai.fraunhofer.de/de/geschaeftsfelder/schnelle-loeser/produkte/samg.html. The necessary information on the numerical method and the simulation setups is provided in the methods section and the references therein (e.g., Weis et al., 2014).

References

Andersen, C., Theissen-Krah, S., Hannington, M., Rüpke, L., & Petersen, S. (2017). Faulting and off-axis submarine massive sulfide accumulation at slow spreading mid-ocean ridges: A numerical modeling perspective. *Geochemistry, Geophysics, Geosystems*, *18*(6), 2305–2320. https://doi.org/10.1002/2017GC006880

Appold, M. S., & Garven, G. (1999). The hydrogeology of ore formation in the Southeast Missouri district: Numerical models of topography-driven fluid flow during the Ouachita orogeny. *Economic Geology*, *94*, 913–935. https://doi.org/10.2113/gsecongeo.94.6.913

Bear, J. (1972). *Dynamics of fluids in porous media (dover civil and mechanical engineering)*. New York. Dover.

Bekins, B. A., McCaffrey, A. M., & Dreiss, S. J. (1995). Episodic and constant flow models for the origin of low-chloride waters in a modern accretionary complex. *Water Resources Research*, *31*(12), 3205–3215. https://doi.org/10.1029/95WR02569

Beranek, L. P. (2017). A magma-poor rift model for the Cordilleran margin of western North America. *Geology*, *45*, 1115–1118. https://doi.org/10.1130/G39265.1

Brenhin Keller, C., Husson, J. M., Mitchell, R. N., Bottke, W. F., Gernon, T. M., Boehnke, P., et al. (2019). Neoproterozoic glacial origin of the great unconformity. In *Proceedings of the National Academy of Sciences of the United States of America*. https://doi.org/10.1073/pnas.1804350116

Campbell, R. W., Beranek, L. P., Piercey, S. J., & Friedman, R. (2019). Early Paleozoic post-breakup magmatism along the Cordilleran margin of western North America: New zircon U-Pb age and whole-rock Nd- and Hf-isotope and lithogeochemical results from the Kechika group, Yukon, Canada. *Geosphere*, *15*(4), 1262–1290. https://doi.org/10.1130/GES02044.1

Cathles, L. M., & Adams, J. J. (2005). Fluid flow and petroleum and mineral resources in the upper (20 km) continental crust. *Economic Geology 100th Anniversary*, 77–110.

Cathles, L. M., & Smith, A. T. (1983). Thermal constraints on the formation of Mississippi Valley-type lead- zinc deposits and their implications for episodic basin dewatering and deposit genesis. *Economic Geology*, *78*(5), 983–1002. https://doi.org/10.2113/gsecongeo.78.5.983

Cecile, M. P., Morrow, D. W., & Williams, G. K. (1997). Early Paleozoic (Cambrian to Early Devonian) tectonic framework, Canadian Cordillera. *Bulletin of Canadian Petroleum Geology*, *45*, 54–74.

Colpron, M., Logan, J. M., & Mortensen, J. K. (2002). U-Pb zircon age constraint for late Neoproterozoic rifting and initiation of the lower Paleozoic passive margin of western Laurentia. *Canadian Journal of Earth Sciences*, *39*(2), 133–143. https://doi.org/10.1139/e01-069

Cook, F. A., Clowes, R. M., Snyder, D. B., van der Velden, A. J., Hall, K. W., Erdmer, P., & Evenchick, C. A. (2004). Precambrian crust beneath the Mesozoic northern Canadian Cordillera discovered by Lithoprobe seismic reflection profiling. *Tectonics*, *23*, TC2010. https://doi.org/10.1029/2002TC001412

Cooke, D. R., Bull, S. W., Large, R. R., & McGoldrick, P. J. (2000). The importance of oxidized brines for the formation of Australian proterozoic stratiform sediment-hosted Pb-Zn (sedex) deposits. *Economic Geology and the Bulletin of the Society of Economic Geologists*, *95*(1), 1–18. https://doi.org/10.2113/gsecongeo.95.1.1

Cox, S. F. (1995). Faulting processes at high fluid pressures: An example of fault valve behavior from the Wattle Gully Fault, Victoria, Australia. *Journal of Geophysical Research*, *100*(B7), 12841–12859. https://doi.org/10.1029/95jb00915

Cox, S. F. (2005). Coupling between deformation, fluid pressures, and fluid flow in ore-producing hydrothermal systems at depth in the crust. In J. W. Hedenquist, J. F. H. Thompson, R. J. Goldfarb, & J. P. Richards (Eds.), *One hundredth anniversary* (pp. 39–75). Society of Economic Geologists. https://doi.org/10.5382/AV100.04

Davidheiser-Kroll, B., Stuart, F. M., & Boyce, A. J. (2014). Mantle heat drives hydrothermal fluids responsible for carbonate-hosted base metal deposits: Evidence from 3He/4He of ore fluids in the Irish Pb-Zn ore district. *Mineralium Deposita*, *49*, 547–553. https://doi.org/10.1007/s00126-014-0516-5

Driesner, T. (2007). The system H2O-NaCl. Part II: Correlations for molar volume, enthalpy, and isobaric heat capacity from 0 to 1000°C, 1 to 5000 bar, and 0 to 1 XNaCl. *Geochimica et Cosmochimica Acta*, *71*(20), 4902–4919. https://doi.org/10.1016/j.gca.2007.05.026

Driesner, T., & Heinrich, C. A. (2007). The system H2O-NaCl. Part I: Correlation formulae for phase relations in temperature-pressure-composition space from 0 to 1000°C, 0 to 5000 bar, and 0 to 1 XNaCl. *Geochimica et Cosmochimica Acta*, *71*(20), 4880–4901. https://doi.org/10.1016/j.gca.2006.01.033

Etschmann, B., Liu, W., Mayanovic, R., Mei, Y., Heald, S., Gordon, R., & Brugger, J. (2019). Zinc transport in hydrothermal fluids: On the roles of pressure and sulfur vs. chlorine complexing. *American Mineralogist*, *104*(1), 158–161. https://doi.org/10.2138/am-2019-6719

Garven, G. (1995). Continental-scale groundwater flow and geologic processes. *Annual Review of Earth and Planetary Sciences*, *23*, 89–117. https://doi.org/10.1146/annurev.ea.23.050195.000513

Garven, G., Bull, S. W., & Large, R. R. (2001). Hydrothermal fluid flow models of stratiform ore genesis in the McArthur Basin, Northern Territory, Australia. *Geofluids*, *1*(4), 289–311. https://doi.org/10.1046/j.1468-8123.2001.00021.x

Ge, S., & Garven, G. (1992). Hydromechanical modeling of tectonically driven groundwater flow with application to the Arkoma Foreland Basin. *Journal of Geophysical Research*, *97*(B6), 9119–9144. https://doi.org/10.1029/92JB00677

Goodfellow, W. D. (2007). Base metal metallogeny of the Selwyn Basin, Canada. In *Base metal metallogeny of the Selwyn Basin, Canada*. In W. D. Goodfellow (Ed.), *Mineral deposits of Canada—A synthesis of major deposit-types, district metallogeny, the evolution of geological provinces, and exploration methods: Geological Survey of Canada* (pp. 553–579).

Goodfellow, W. D., Cecile, M., & Leybourne, M. (1995). Geochemistry, petrogenesis, and tectonic setting of Lower Paleozoic alkalic and potassic volcanic rocks, Northern Canadian Cordilleran Miogeocline. *Canadian Journal of Earth Sciences*, *32*, 2167. https://doi.org/10.1139/e95-169

Goodfellow, W. D., & Lydon, J. W. (2007). Sedimentary exhalative (SEDEX) deposits. In W. D. Goodfellow (Ed.), *Mineral deposits of Canada: A synthesis of major deposit-types, district metallogeny, the evolution of geological provinces, and exploration* (pp. 163–183). Geological Association of Canada, Mineral Deposits Division, Special Publication No.

Gordey, S. P., & Anderson, R. G. (1993). *Evolution of the northern cordilleran miogeocline, Nahanni map area (105I), Yukon and Northwest Territories*. Geological Survey of Canada.Memoir 428.

Hart, N. R., Stockli, D. F., Lavier, L. L., & Hayman, N. W. (2017). Thermal evolution of a hyperextended rift basin, Mauléon Basin, western Pyrenees. *Tectonics*, *36*(6), 1103–1128. https://doi.org/10.1002/2016TC004365

Heinrich, C. A., & Candela, P. A. (2014). Fluids and Ore Formation in the Earth's Crust. In H. D. Holland, & K. K. Turekian (Eds.), *Treatise on Geochemistry* (2nd ed., pp. 1–28). Oxford: Elsevier. https://doi.org/10.1016/B978-0-08-095975-7.01101-3

Hoggard, M. J., Czarnota, K., Richards, F. D., Huston, D. L., Jaques, A. L., & Ghelichkhan, S. (2020). Global distribution of sediment-hosted metals controlled by craton edge stability. *Nature Geoscience*, *13*, 504–510. https://doi.org/10.1038/s41561-020-0593-2

Hunt, J. M. (1990). Generation and migration of petroleum from abnormally pressured fluid compartments. *American Association of Petroleum Geologists Bulletin*, *74*(1). https://doi.org/10.1306/0c9b27e5-1710-11d7-8645000102c1865d

Hyndman, R. D. (2010). The consequences of Canadian Cordillera thermal regime in recent tectonics and elevation: A review. *Canadian Journal of Earth Sciences*, *47*(5), 621–632. https://doi.org/10.1139/E10-016

Ingebritsen, S. E., & Appold, M. S. (2012). The physical hydrogeology of ore deposits. *Economic Geology*, *107*(4), 559–584. https://doi.org/10.2113/econgeo.107.4.559

Ingebritsen, S. E., & Gleeson, T. (2015). Crustal permeability: Introduction to the special issue. *Geofluids*, *15*(1–2). https://doi.org/10.1111/gfl.12118

Ingebritsen, S. E., & Manning, C. E. (2010). Permeability of the continental crust: Dynamic variations inferred from seismicity and metamorphism. *Geofluids*, *10*(1–2), 193–205. https://doi.org/10.1111/j.1468-8123.2010.00278.x

Ingebritsen, S. E., Sanford, W. E., & Neuzil, C. E. (2006). *Groundwater in geologic processes* (2nd ed.). Cambridge University Press.

Jackson, J. A. (1987). Active normal faulting and crustal extension. *Geological Society, London, Special Publications*, *28*(1), 3–17. https://doi.org/10.1144/gsl.sp.1987.028.01.02

Large, R. R., Bull, S. W., McGoldrick, P. J., Walters, S., Derrick, G. M., & Carr, G. R. (2005). Strata-Bound and Stratiform Zn-Pb-Ag Deposits in Proterozoic Sedimentary Basins, Northern Australia. In *Economic Geology 100th Anniversary*.

Leach, D., Bradley, D., Huston, D., Pisarevsky, S., Taylor, R., & Gardoll, S. (2010). Sediment-hosted lead-zinc deposits in Earth history. *Economic Geology*, *105*, 593–625. https://doi.org/10.2113/gsecongeo.105.3.593

Lewis, T. J., Hyndman, R. D., & Flück, P. (2003). Heat flow, heat generation, and crustal temperatures in the northern Canadian Cordillera: Thermal control of tectonics. *Journal of Geophysical Research*, *108*(B6), 2316. https://doi.org/10.1029/2002jb002090

Li, F., Sun, Z., Pang, X., Liao, J., Yang, H., Xie, H., et al. (2019). Low-viscosity crustal layer controls the crustal architecture and thermal distribution at hyper-extended margins: Modeling insight and application to the northern South China Sea margin. *Geochemistry, Geophysics, Geosystems*, *20*, 3248–3267. https://doi.org/10.1029/2019GC008200

Lund, K. (2008). Geometry of the Neoproterozoic and Paleozoic rift margin of western Laurentia: Implications for mineral deposit settings. *Geosphere*, *4*(2), 429–444. https://doi.org/10.1130/GES00121.1

Lydon, J. W. (2015). The leachability of metals from sedimentary rocks. In S. Paradis (Ed.), *Targeted geoscience initiative 4: Sediment-hosted Zn-Pb deposits: Processes and implications for exploration* Open File 7838, (11–42). https://doi.org/10.4095/296328

Magnall, J. M., Gleeson, S. A., Blamey, N. J. F., Paradis, S., & Luo, Y. (2016). The thermal and chemical evolution of hydrothermal vent fluids in shale hosted massive sulphide (SHMS) systems from the MacMillan Pass district (Yukon, Canada). *Geochimica et Cosmochimica Acta*, *193*, 251–273. https://doi.org/10.1016/j.gca.2016.07.020

Magnall, J. M., Gleeson, S. A., & Paradis, S. (2020). A new subseafloor replacement model for the Macmillan pass clastic-dominant Zn-Pb ± Ba deposits (Yukon, Canada). *Economic Geology*, *115*, 953–959. https://doi.org/10.5382/econgeo.4719

Manga, M., Beresnev, I., Brodsky, E. E., Elkhoury, J. E., Elsworth, D., Ingebritsen, S. E., et al. (2012). Changes in permeability caused by transient stresses: Field observations, experiments, and mechanisms. *Reviews of Geophysics*, *50*(2). https://doi.org/10.1029/2011RG000382

Manning, A. H., & Emsbo, P. (2018). Testing the potential role of brine reflux in the formation of sedimentary exhalative (sedex) ore deposits. *Ore Geology Reviews*, *102*, 862–874. https://doi.org/10.1016/j.oregeorev.2018.10.003

Martel, E., Turner, E. C., & Fischer, B. J. (2011). Geology of the central Mackenzie Mountains of the northern Canadian Cordillera, Sekwi Mountain (105P), Mount Eduni (106A), and northwestern Wrigley Lake (95M) map-areas, Northwest Territories. *NWT Special*, *1*(1), 413.

Morley, C. K. (1995). Developments in the structural geology of rifts over the last decade and their impact on hydrocarbon exploration. *Geological Society, London, Special Publications*, *80*(1), 1–32. https://doi.org/10.1144/gsl.sp.1995.080.01.01

Moynihan, D., Strauss, J., Nelson, L., & Padget, C. (2019). Upper windermere supergroup and the transition from rifting to continent-margin sedimentation, Nadaleen River area, northern Canadian Cordillera. *Geological Society of America Bulletin*, *131*, 1673–1701. https://doi.org/10.1130/B32039.1

Muchez, P., Heijlen, W., Banks, D., Blundell, D., Boni, M., & Grandia, F. (2005). 7: Extensional tectonics and the timing and formation of basin-hosted deposits in Europe. *Ore Geology Reviews*, *27*, 241–267. https://doi.org/10.1016/j.oregeorev.2005.07.013

Neuzil, C. E. (2019). Permeability of clays and shales. *Annual Review of Earth and Planetary Sciences*, *47*, 247–273. https://doi.org/10.1146/annurev-earth-053018-060437

Oliver, N. H. S., McLellan, J. G., Hobbs, B. E., Cleverley, J. S., Ord, A., & Feltrin, L. (2006). Numerical models of extensional deformation, heat transfer, and fluid flow across basement-cover interfaces during basin-related mineralization. *Economic Geology*, *101*(1), 1–31. https://doi.org/10.2113/101.1.110.2113/gsecongeo.101.1.1

Pérez-Gussinyé, M., Reston, T. J., & Phipps Morgan, J. (2001). Serpentinization and magmatism during extension at non-volcanic margins: The effect of initial lithospheric structure. *Geological Society, London, Special Publications*, *187*(1), 551–576. https://doi.org/10.1144/GSL.SP.2001.187.01.27

Peron-Pinvidic, G., Manatschal, G., & the "IMAGinING RIFTING Workshop Participants (2019). Rifted margins: State of the art and future challenges. *Frontiers in Earth Science*, *7*, 218. https://doi.org/10.3389/feart.2019.00218

Phillips, O. M. (1991). *Flow and reactions in permeable rocks*. Cambridge. Cambridge University Press.

Powley, D. E. (1990). Pressures and hydrogeology in petroleum basins. *Earth-Science Reviews*, *29*(1–4), 215–226. https://doi.org/10.1016/0012-8252(0)90038-W

Rajabi, A., Canet, C., Rastad, E., & Alfonso, P. (2014). Basin evolution and stratigraphic correlation of sedimentary-exhalative Zn– Pb deposits of the Early Cambrian Zarigan– Chahmir Basin, Central Iran. *Ore Geology Reviews*, *64*, 328–353. https://doi.org/10.1016/j.oregeorev.2014.07.013

Ranganathan, V. (1992). Basin dewatering near salt domes and formation of brine plumes. *Journal of Geophysical Research*, *97*(B4), 4667. https://doi.org/10.1029/91JB03082

Ranganathan, V., & Hanor, J. S. (1989). Perched brine plumes above salt domes and dewatering of geopressured sediments. *Journal of Hydrology*, *110*(1–2), 63–86. https://doi.org/10.1016/0022-1694(89)90237-0

Roberts, S. J., Nunn, J. A., Cathles, L., & Cipriani, F. D. (1996). Expulsion of abnormally pressured fluids along faults. *Journal of Geophysical Research: Solid Earth*, *101*(12), 28231–28252. https://doi.org/10.1029/96jb02653

Saffer, D. M. (2015). The permeability of active subduction plate boundary faults. *Geofluids*, *15*(1–2). https://doi.org/10.1111/gfl.12103

Sangster, D. F. (2018). Toward an integrated genetic model for vent-distal SEDEX deposits. *Mineralium Deposita*, *53*(4), 509–527. https://doi.org/10.1007/s00126-017-0755-3

Sibson, R. H., Robert, F., & Poulsen, K. H. (1988). High-angle reverse faults, fluid-pressure cycling, and mesothermal gold-quartz deposits. *Geology*, *16*(6). https://doi.org/10.1130/0091-7613(1988)016<0551:harffp>2.3.co;2

Simms, M. A., & Garven, G. (2004). Thermal convection in faulted extensional sedimentary basins: Theoretical results from finite-element modeling. *Geofluids*, *4*(2), 109–130. https://doi.org/10.1111/j.1468-8115.2004.00069.x

Strauss, J., MacDonald, F., Halverson, G., Tosca, N., Schrag, D., & Knoll, A. (2015). Stratigraphic evolution of the Neoproterozoic Callison Lake Formation: Linking the break-up of Rodinia to the Islay carbon isotope excursion. *American Journal of Science*, *315*, 881–944. https://doi.org/10.2475/10.2015.01

Turner, R. J. W. (1992). Bedded barite deposits in the United States, Canada, Germany, and China; two major types based on tectonic setting; a discussion. *Economic Geology*, *87*(1), 198–200. https://doi.org/10.2113/gsecongeo.87.1.198

Walsh, J. J., Torremans, K., Guven, J., Kyne, R., Conneally, J., & Bonson, C. (2018). *Fault-Controlled Fluid Flow within extensional basins and its Implications for sedimentary rock-hosted mineral deposits* (pp. 237–269). https://doi.org/10.5382/sp.21.11

Weis, P., Driesner, T., Coumou, D., & Geiger, S. (2014). Hydrothermal, multiphase convection of H2O-NaCl fluids from ambient to magmatic temperatures: A new numerical scheme and benchmarks for code comparison. *Geofluids*, *14*, 347–371. https://doi.org/10.1111/gfl.12080

Weis, P., Driesner, T., & Heinrich, C. A. (2012). Porphyry-copper ore shells form at stable pressure-temperature fronts within dynamic fluid plumes. *Science*, *338*(6114), 1613–1616. https://doi.org/10.1126/science.1225009

Wilkinson, J. J. (2014). 13.9 - Sediment-Hosted Zinc–Lead Mineralization: Processes and Perspectives. In H. D. Holland & K. K. Turekian (Eds.), *Treatise on Geochemistry* (2nd ed.) (pp. 219–249). Oxford. Elsevier. https://doi.org/10.1016/B978-0-08-095975-7.01109-8

Yang, J., Large, R. R., Bull, S., & Scott, D. L. (2006). Basin-scale numerical modeling to test the role of buoyancy-driven fluid flow and heat transfer in the formation of stratiform Zn-Pb-Ag deposits in the Northern Mount Isa Basin. *Economic Geology*, *101*(6), 1275–1292. https://doi.org/10.2113/gsecongeo.101.6.1275

Yang, J., Large, R. R., & Bull, S. W. (2004). Factors controlling free thermal convection in faults in sedimentary basins: Implications for the formation of zinc–lead mineral deposits. *Geofluids*, *4*(3), 237–247. https://doi.org/10.1111/j.1468-8123.2004.00084.x

Yao, Q., & Demicco, R. V. (1997). Dolomitization of the Cambrian carbonate platform, southern Canadian rocky mountains: Dolomite front geometry, fluid inclusion geochemistry, isotopic signature, and hydogeologic modelling studies. *American Journal of Science*, *297*(9), 892–938. https://doi.org/10.2475/ajs.297.9.892

Yapparova, A., Gabellone, T., Whitaker, F., Kulik, D. A., & Matthäi, S. K. (2017a). Reactive Transport Modelling of Dolomitisation Using the New CSMP++GEM Coupled Code: Governing Equations, Solution Method and Benchmarking Results. *Transport in Porous Media*, *117*(3), 385–413. https://doi.org/10.1007/s11242-017-0839-7

Yapparova, A., Gabellone, T., Whitaker, F., Kulik, D. A., & Matthäi, S. K. (2017b). Reactive transport modelling of hydrothermal dolomitisation using the CSMP++GEM coupled code: Effects of temperature and geological heterogeneity. *Chemical Geology*, *466*, 562–574. https://doi.org/10.1016/j.chemgeo.2017.07.005

Yardley, B. W. D. (2005). Metal concentrations in crustal fluids and their relationship to ore formation. *Economic Geology*, *100*, 613–632. https://doi.org/10.2113/100.4.613

Yonkee, W. A., Dehler, C. D., Link, P. K., Balgord, E. A., Keeley, J. A., Hayes, D. S., et al. (2014). Tectono-stratigraphic framework of Neoproterozoic to Cambrian strata, west-central U.S.: Protracted rifting, glaciation, and evolution of the North American Cordilleran margin. *Earth-Science Reviews*, *136*, 59–95. https://doi.org/10.1016/j.earscirev.2014.05.004

Zhong, R., Brugger, J., Chen, Y., & Li, W. (2015). Contrasting regimes of Cu, Zn and Pb transport in ore-forming hydrothermal fluids. *Chemical Geology*, *395*, 154–164. https://doi.org/10.1016/j.chemgeo.2014.12.008

References From the Supporting Information

Audétat, A., Günter, D., & Heinrich, C. A. (2000). Causes for large-scale metal zonation around mineralized. *Economic Geology*, *95*, 1563–1581. https://doi.org/10.2113/95.8.1563

Banks, D. A., Davies, G. R., Yardley, B. W. D., McCaig, A. M., & Grant, N. T. (1991). The chemistry of brines from Alpine thrust system in the Central Pyrenees: An application of fluid inclusion analysis to the study of fluid behaviour in orogenesis. *Geochimica et Cosmochimica Acta*, *55*, 1021–1030. https://doi.org/10.1016/0016-7037(91)90160-7

Banks, D. A., Guiliani, G., Yardley, B. W. D., & Cheilletz, A. (2000). Emerald mineralization in Colombia: Fluid chemistry and the role on brine mixing. *Mineralium Deposita*, *35*, 699–713. https://doi.org/10.1007/s001260050273

Campbell, A. R., Banks, D. A., Phillips, R. S., & Yardley, B. W. D. (1995). Geochemistry of the Th-U-REE mineralizing magmatic fluids, Captain Mountains, New Mexico. *Economic Geology*, *90*, 1271–1287. https://doi.org/10.2113/gsecongeo.90.5.1271

Carpenter, A. B., Trout, M. L., & Pickett, E. E. (1974). Preliminary report on the origin and chemical evolution of lead- and zinc-rich oil-field brines in Central Mississippi. *Economic Geology*, *69*, 1191–1206. https://doi.org/10.2113/gsecongeo.69.8.1191

Connolly, C. A., Walter, L. M., Baadsgaard, H., & Longstaffe, F. J. (1990). Origin and evolutions of formation waters, Alberta basin, western Canada sedimentary basin. I. Chemistry. *Applied Geochemistry*, *5*, 375–395. https://doi.org/10.1016/0883-2927(90)90016-x

Frape, S. K., & Fritz, B. (1987). *Geochemical trends from groundwaters from the Canadian Shield*. Geological Association of Canada Special Paper.(pp. 19–38).

Heinrich, C. A., Ryan, C. G., Mernach, T. P., & Eadington, P. J. (1992). Segregation of ore metals between magmatic brine and vapor: A fluid inclusion study using PIXIE microanalysis. *Economic Geology*, *87*, 1566–1583. https://doi.org/10.2113/gsecongeo.87.6.1566

Kamenetsky, V. S., Achterbergh, E. A., Ryan, C. G., Naumov, V. B., Mernagh, T. P., & Davidson, P. (2002). Extreme heterogeneity of granite-derived hydrothermal fluids: An example from inclusions in a single crystal of miarolitic quartz. *Geology*, *30*, 459–462. https://doi.org/10.1130/0091-7613(2002)030<0459:echogd>2.0.co;2

Land, L. S., Macpherson, G. L., & Mack, L. E. (1988). The geochemistry of saline formation waters, Miocene, offshore Louisiana. *Gulf Coast Association of Geological Societes, Transactions*, *38*, 503–511. https://doi.org/10.1306/a1addbed-0dfe-11d7-8641000102c1865d

McCaig, A. M., Tritlla, J., & Banks, D. A. (2000). Fluid mixing and recycling during Pyrenean thrusting: Evidence from fluid inclusion halogen ratios. *Geochimica et Cosmochimica Acta*, *64*, 3395–3412. https://doi.org/10.1016/s0016-7037(00)00437-3

Meere, P. A., & Banks, D. A. (1997). Upper crustal fluid migration: An example from the Variscides of SW Ireland. *Journal of the Geological Society of London*, *154*, 975–985. https://doi.org/10.1144/gsjgs.154.6.0975

Munz, L. A., Yardley, B. W. D., Banks, D. A., & Wayne, D. (1995). Deep penetration of sedimentary fluids in basement rocks from southern Norway: Evidence from hydrocarbon and brine inclusions in quartz veins. *Geochimica et Cosmochimica Acta*, *59*, 239–254. https://doi.org/10.1016/0016-7037(94)00322-d

Pike, S. (1993). *The chemistry of granite derived pegmatite fluids* (p. 244). Unpublished Ph. D. thesis. University of Leeds.

Smith, M. P., Banks, D. A., Yardley, B. W. D., & Boyce, A. (1996). Fluid inclusion and stable isotope constrains on the genesis of the Cligga Head Sn-W deposit, S.W. England. *European Journal of Mineralogy*, *8*, 961–974. https://doi.org/10.1127/ejm/8/5/0961

Williams, A. E., & McKibben, M. A. (1989). A brine interface in the Salton Sea geothermal system, California: Fluid geochemical and isotopic characteristics. *Geochimica et Cosmochimica Acta*, *53*, 1905–1920. https://doi.org/10.1016/0016-7037(89)90312-8

Yardley, B. W. D., Banks, D. A., Bottrell, S. H., & Diamond, L. W. (1993). The composition and origin of the ore fluid. *Mineralogical Magazine*, *57*, 407–422. https://doi.org/10.1180/minmag.1993.057.388.05